


 Cite this: *RSC Adv.*, 2022, 12, 31757

Photoluminescence and afterglow of Dy³⁺ doped CaAl₂O₄ derived *via* sol–gel combustion†

 Bao-gai Zhai, Meng Meng Chen  and Yuan Ming Huang *

With doping concentration varying from 0.1 to 5.0 mol%, a series of Dy³⁺ doped calcium aluminate (CaAl₂O₄:Dy³⁺) phosphors were synthesized *via* a sol–gel combustion technique. The phase, morphology, photoluminescence (PL), afterglow, and thermoluminescence (TL) glow curves of CaAl₂O₄:Dy³⁺ were investigated by means of X-ray diffractometry, scanning electron microscopy, transmission electron microscopy, PL spectroscopy, afterglow spectroscopy, and TL dosimetry, respectively. It is found that: (i) oxygen vacancies and Dy³⁺ work as two independent sets of luminescence centers of PL for CaAl₂O₄:Dy³⁺; (ii) Dy³⁺ works as the luminescence center of afterglow for CaAl₂O₄:Dy³⁺; (iii) the afterglow of CaAl₂O₄:Dy³⁺ lasts for about 115 min at the optimal doping concentration of around 0.8 mol%; and (iv) multiple traps, which are sensitive to doping concentration, are present in CaAl₂O₄:Dy³⁺. The PL and afterglow mechanisms of CaAl₂O₄:Dy³⁺ are discussed to reveal the processes of charged carrier excitation, migration, trapping, detrapping, and radiative recombination in CaAl₂O₄:Dy³⁺.

 Received 10th August 2022
 Accepted 1st November 2022

DOI: 10.1039/d2ra05008k

rsc.li/rsc-advances

1. Introduction

Rare-earth doped calcium aluminate phosphors have been intensively studied due to their excellent afterglow properties,^{1–4} among which Dy³⁺ doped calcium aluminate (CaAl₂O₄:Dy³⁺) is a well-known inorganic phosphor which emits white photoluminescence (PL) under ultraviolet excitation.⁵ Apart from its white PL, CaAl₂O₄:Dy³⁺ exhibits a white afterglow even after the removal of ultraviolet excitation.⁶ As reported by Liu *et al.* in 2005, Dy³⁺ works as the luminescence center of afterglow for CaAl₂O₄:Dy³⁺ and the white afterglow of solid state reaction derived CaAl₂O₄:Dy³⁺ lasts 32 min at the optimal doping concentration of 2 at%.⁶ For afterglow materials, the processes of charged carrier excitation, migration, trapping, detrapping, and radiative recombination are critically important to understand their afterglow properties.^{7–9} For example, long afterglow can be achieved at room temperature only when traps have an appropriate activation energy somewhere around 0.65 eV whereas shallow traps ($E \leq 0.4$ eV) and deep traps ($E > 2$ eV) are not favorable because they can be emptied either easily or with difficulty at room temperature.⁷ Up to date, only a single report exists on the afterglow of CaAl₂O₄:Dy³⁺, leaving the processes of charged carrier excitation, migration, trapping and detrapping not fully revealed. The lack of such knowledge hampers the

comprehensive understanding of the afterglow mechanism of CaAl₂O₄:Dy³⁺.

With respect to solid state reaction derived CaAl₂O₄:Dy³⁺, sol–gel combustion derived CaAl₂O₄:Dy³⁺ is abundant in oxygen and calcium vacancies. In CaAl₂O₄:Dy³⁺, oxygen vacancies are potential electron traps because they are positively charged whereas calcium vacancies are potential hole traps because they are negatively charged.^{8,10} Therefore, sol–gel combustion derived CaAl₂O₄:Dy³⁺ phosphors are suitable for exploring the afterglow mechanisms of CaAl₂O₄:Dy³⁺. In this paper, we report the PL and afterglow properties of sol–gel combustion derived CaAl₂O₄:Dy³⁺ with the doping concentrations varying from 0.1 to 5.0 mol%. A picture on the PL and afterglow mechanisms of CaAl₂O₄:Dy³⁺ is given to reveal the processes of charged carriers' excitation, migration, trapping, detrapping, and recombination in CaAl₂O₄:Dy³⁺.

2. Experimental section

2.1 Sol–gel combustion synthesis of CaAl₂O₄:Dy³⁺

CaAl₂O₄:Dy³⁺ phosphors with the doping concentrations varying from 0.1 to 5.0 mol% were synthesized *via* the sol–gel combustion with urea as fuel.^{11–13} All reagents were in analytical grade and provided by Sinopharm Chemical Reagents Co., Ltd (Shanghai, China). The purity of dysprosium oxide (Dy₂O₃) was 99.99%. Under stirring with a magnetic bar, Ca(NO₃)₂·4H₂O (0.2 mol), Al(NO₃)₃·9H₂O (0.4 mol), urea (6.0 mol), H₃BO₃ (0.02 mol) and stoichiometric amount of Dy₂O₃ were dissolved in deionized water (600 mL) to form a transparent solution. A homogeneous solution was obtained after the mixture was

School of Microelectronics and Control Engineering, Changzhou University, Changzhou 213164, China. E-mail: dongshanisland@126.com

† Electronic supplementary information (ESI) available. See DOI: <https://doi.org/10.1039/d2ra05008k>



stirred vigorously for 60 min in a glass beaker. After having been aged at room temperature for two weeks, the solution was ready for the sol-gel combustion. Urea and boric acid functioned as the fuel and flux, respectively. Alumina crucibles, each with the volume capacity of 50 mL, were employed as the reaction containers. Half filled with the aged solution, the solution-containing alumina crucible was transferred into an air-filled box furnace for self-propagating combustion. The temperature in the furnace was preset at 780 °C. After the solution-containing crucible was transferred into the furnace, the temperature in the furnace was gradually dropped to about 706 °C. Heated at such high temperatures, water in the solution got boiling and the starting materials (fuels and metal nitrates) in the crucible were partially decomposed until the organic fuels were automatically ignited to initiate the exothermic reactions. The sol-gel combustion yielded voluminous gases and bright flames. In this work, the synthesis was initiated by point-heating of a small part of the mixture in the crucible, and the ignition was started at around 750 °C. Once started, a wave of exothermic reactions swept through the remaining material in the crucible. This combustion synthesis lasted for about 40 s, which was exceptionally fast when compared to high-temperature solid state reactions. During the sol-gel combustion, a large amount of energy was released from the exothermic reactions, which in turn raised the temperature in the furnace up to 830 °C. Measured with an infrared thermometer, the temperature in the flame was up to 1300 °C. After the fire was extinguished, the crucible was taken out of the furnace immediately. The total holding time of the crucible in the furnace was about 4 min. White powders were resulted after the sol-gel combustion. According to molar ratio of Dy^{3+} to Ca^{2+} in the starting materials, a series of $\text{CaAl}_2\text{O}_4:\text{Dy}^{3+}$ phosphors were obtained with the nominal doping concentration of Dy^{3+} varying in the range of 0.1–5.0 mol%. No further calcination was applied to the sol-gel combustion derived $\text{CaAl}_2\text{O}_4:\text{Dy}^{3+}$.

2.2 Solid state synthesis of $\text{CaAl}_2\text{O}_4:\text{Dy}^{3+}$ phosphors

For comparison, solid state reaction derived $\text{CaAl}_2\text{O}_4:\text{Dy}^{3+}$ phosphors were synthesized with CaCO_3 (0.02 mol), Al_2O_3 (0.02 mol), H_3BO_3 (0.002 mol), Dy_2O_3 as raw materials. Stoichiometric mixtures of the raw materials were homogeneously mixed and ground. Subsequently the mixture was transferred into alumina crucibles and sintered at 900 °C for 4 h in an air-filled electric tube furnace. The sintered products were ground again in an agate mortar, then the powder products were calcined at 1350 °C for 10 h in air. According to the molar ratio of Dy^{3+} to Ca^{2+} in the starting materials, the doping concentration of Dy^{3+} in the solid state reaction derived $\text{CaAl}_2\text{O}_4:\text{Dy}^{3+}$ varied in the range 0.1–10.0 mol%.

2.3 Phase, morphology and elemental composition of $\text{CaAl}_2\text{O}_4:\text{Dy}^{3+}$ phosphors

X-Ray diffraction (XRD) profiles of $\text{CaAl}_2\text{O}_4:\text{Dy}^{3+}$ phosphors were recorded on X-ray diffractometer (D/max 2500 PC, Rigaku Corporation, Akishima, Japan) using $\text{Cu K}\alpha$ radiation ($\lambda = 0.15405$ nm). The scanning electron microscope (SEM) (model

S-4800, Hitachi, Tokyo, Japan) was employed to analyze the morphology of the synthesized products. The SEM was coupled with a silicon drifted detector as the X-ray analyzer to record the energy dispersive X-ray (EDX) spectrum of the synthesized products. The micrographs of $\text{CaAl}_2\text{O}_4:\text{Dy}^{3+}$ nanocrystals were recorded on a transmission electron microscope (TEM) (model JEOL JEM-2100, Japan Electronics Corp, Akishima, Japan). Samples for TEM analysis were prepared by suspending the particles in ethanol under the excitation of ultrasonification and then drying a drop of the suspension on a carbon-coated copper grid.

2.4 PL excitation and emission spectra of $\text{CaAl}_2\text{O}_4:\text{Dy}^{3+}$

The PL excitation spectrum of $\text{CaAl}_2\text{O}_4:\text{Dy}^{3+}$ was measured with the fluorescence spectrometer F-7000 (Hitachi, Japan). The spectrophotometer (Tianjin Gangdong Ltd., Tianjin, China) was used to acquire the steady-state PL spectra of $\text{CaAl}_2\text{O}_4:\text{Dy}^{3+}$. The excitation source of the PL spectrum was provided by a helium-cadmium laser (Kimmon Electric Co. Ltd., Tokyo, Japan). The emission wavelength and the output power of the laser radiation were 325 nm and 13 mW, respectively.

2.5 Afterglow spectra and thermoluminescence (TL) glow curves of $\text{CaAl}_2\text{O}_4:\text{Dy}^{3+}$

The afterglow spectra of $\text{CaAl}_2\text{O}_4:\text{Dy}^{3+}$ were recorded with the PL spectrophotometer (Tianjin Gangdong Ltd, Tianjin, China) immediately after the ultraviolet irradiation of a high-pressure mercury lamp was blocked off. The output power of the high-pressure mercury lamp was 175 W. The irradiation duration of the high-pressure lamp irradiation was 3 min. Afterglow decay curve was taken by focusing the afterglows into the entrance slit of the spectrometer. The TL glow curves of $\text{CaAl}_2\text{O}_4:\text{Dy}^{3+}$ were measured on a TL meter constructed according to the scheme given by Yamashita *et al.*¹⁴ The phosphor was placed on an electrically heated plate, the temperature of the plate was controlled with a program in computer. As the temperature of the plate was raised linearly with time, the light output of the phosphor was recorded using a photomultiplier in a photon-counting mode. A bi-alkali photomultiplier tube (model H10425, Hamamatsu, Japan) was used in the TL meter for the luminescence detection, it covers the 350–600 nm wavelength range. Prior to the TL measurements, $\text{CaAl}_2\text{O}_4:\text{Dy}^{3+}$ phosphors were exposed to the 254 nm irradiation of a low-pressure mercury lamp for 5 min. The output power of the low-pressure mercury lamp was 32 W. The TL signals of $\text{CaAl}_2\text{O}_4:\text{Dy}^{3+}$ phosphors were recorded when the $\text{CaAl}_2\text{O}_4:\text{Dy}^{3+}$ phosphors were heated from 10 to 200 °C at a rate of 2 °C s^{-1} .

3. Results and discussions

3.1 Phase and morphology of $\text{CaAl}_2\text{O}_4:\text{Dy}^{3+}$

Fig. 1 represents the XRD profiles of $\text{CaAl}_2\text{O}_4:\text{Dy}^{3+}$ with different doping concentrations. The XRD data of monoclinic CaAl_2O_4 registered in Joint Committee on Powder Diffraction Standards (JCPDS) card no. 23-1306 are depicted at the bottom of the figure for comparison. The scale of the intensity of powder X-ray



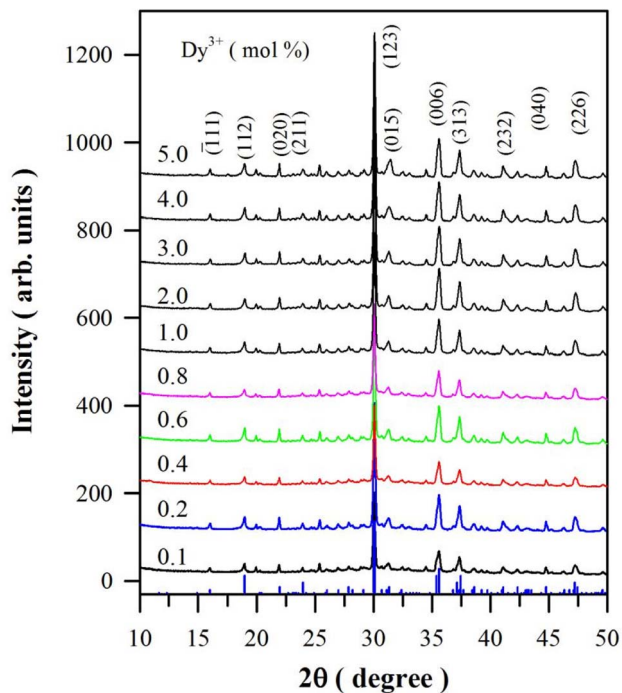


Fig. 1 XRD curves of $\text{CaAl}_2\text{O}_4:\text{Dy}^{3+}$ with doping concentrations varying from 0.1 to 5.0 mol%. The standard diffraction data of CaAl_2O_4 (JCPDS 23-1036) are displayed at the bottom of this figure for comparison.

diffraction is counts of photons received by the detector. For the purpose of clarity, the XRD curves in Fig. 1 are evenly spaced after having been shifted upwards one by one, so the scale of the intensity of powder XRD in Fig. 1 is arbitrary units. As can be seen in Fig. 1, each XRD profile of $\text{CaAl}_2\text{O}_4:\text{Dy}^{3+}$ exhibits distinct peaks at $2\theta = 16.01, 18.99, 21.98, 23.97, 30.08, 31.35, 35.63, 37.46, 41.11, 44.76$ and 47.24° . According to the diffraction data registered in JCPDS card no. 23-1036, these peaks can be attributed to the X-ray diffractions from crystallographic planes ($\bar{1}11$), (112), (020), (211), (123), (015), (006), (313), (232), (040) and (226) of monoclinic CaAl_2O_4 , respectively. Among these peaks, the strongest one is located at 30.08° and indexed as (123). Actually, this peak is contributed jointly by two crystallographic planes (220) and (123) of monoclinic CaAl_2O_4 , which are located at $2\theta = 30.11$ and 30.05° , respectively. Being closely packed and nearly equal in diffraction intensity, the two peaks are not distinguishable in the XRD profiles. This is the reason why some researchers indexed the peak at around 30.8° as (220).^{7,8} Obviously, the diffraction peaks in Fig. 1 match well with the standard XRD diffractograms of monoclinic CaAl_2O_4 .^{3,15,16} Furthermore, these peaks are found to agree well with the calculated XRD diffractograms of monoclinic CaAl_2O_4 (Fig. S1†). The absence of a secondary phase in the XRD profiles indicates that Dy^{3+} ions are successfully incorporated into CaAl_2O_4 without introducing new phase in the crystal structure when doping concentration is lower than 5.0 mol%. For sol-gel combustion, nitrate forms of starting materials are highly necessary. Instead of Dy_2O_3 , for example, $\text{Dy}(\text{NO}_3)_3$ is favored as the starting material. It is known that Dy_2O_3 can be dissolved

into dilute HNO_3 solution to form $\text{Dy}(\text{NO}_3)_3$.⁹ In this work, Dy_2O_3 is used as a starting material to provide the source of Dy^{3+} because a tiny amount of Dy_2O_3 can be dissolved into the aqueous solution of $\text{Al}(\text{NO}_3)_3$ and urea after stirring with a magnetic bar for a couple of hours at a temperature higher than 20°C . Since the synthesis process occurs at high temperatures generated by the self-propagating combustion, this method is ideally suited for the production of refractory materials including ceramics CaAl_2O_4 .

Monoclinic CaAl_2O_4 is known to have the stuffed tridymite structure with the space group $P2_1/n$ and $Z = 12$. Fig. S2(a)† displays the conventional unit cell of monoclinic CaAl_2O_4 . Taken from the Inorganic Crystal Structure Database (ICSD), the lattice parameters of monoclinic CaAl_2O_4 ($a = 0.8694$ nm, $b = 0.8093$ nm, $c = 1.5210$ nm, and $\beta = 90.1665^\circ$) are used to construct the crystal structure in present work (ICSD #159925). Obviously, this unit cell consists of 12 Ca sites, 24 Al sites and 48 O sites. As labeled as sites Ca1, Ca2 and Ca3 in Fig. S2(a)†, there are three crystallographically different sites for Ca^{2+} in the unit cell of CaAl_2O_4 . Two of the Ca sites are six-coordinated and one Ca site is nine-coordinated.¹⁷ In monoclinic CaAl_2O_4 , a three-dimensional network is formed by corner-sharing $[\text{AlO}_4]$ tetrahedra, the Ca^{2+} ions are located along the channels in b -direction. Fig. S2(b)† illustrates the schematic view of the monoclinic CaAl_2O_4 along the b -direction. Such a crystal structure makes it easy for Dy^{3+} ions to substitute the Ca^{2+} sites in CaAl_2O_4 . The effective ionic radii of cations depend on their coordination numbers (CN). In the case of site occupancy, the effective ionic radii of Ca^{2+} are 0.100 nm (CN = 6) and 0.118 nm (CN = 9), the effective ionic radii of Dy^{3+} are 0.091 nm (CN = 6) and 0.108 nm (CN = 9).¹⁸ Due to the comparable ionic sizes, Dy^{3+} ions tend to replace the Ca^{2+} ions in the lattice of CaAl_2O_4 .

Fig. 2(a) displays the SEM micrograph of sol-gel combustion derived $\text{CaAl}_2\text{O}_4:\text{Dy}^{3+}$ (5.0 mol%). As shown in Fig. 2(a), the sol-gel combustion derived $\text{CaAl}_2\text{O}_4:\text{Dy}^{3+}$ phosphors are in the form of irregular aggregates with their dimensions up to $20\ \mu\text{m}$. Sol-gel combustion derived aluminate nanocrystals are prone to forming large aggregates. Micrometer-sized pores are randomly distributed in the aggregates due to the production of a large amount of gases during the reaction.^{3,8,11-13,19,20} Fig. 2(b) shows the SEM micrographs of $\text{CaAl}_2\text{O}_4:\text{Dy}^{3+}$ to display the channels formed in the aggregates, each scale bar represents $2\ \mu\text{m}$. It is evident that channels with different diameters are present in the aggregate. Fig. 2(c) shows the TEM micrograph of the $\text{CaAl}_2\text{O}_4:\text{Dy}^{3+}$. Obviously, each aggregate consists of a large number of nanocrystals. Previous work has evidenced that one aggregate consists of a number of nanocrystals whose sizes vary from 10 nm to 80 nm.^{4,16,17,21} As a contrast, solid state reaction derived $\text{CaAl}_2\text{O}_4:\text{Dy}^{3+}$ exhibits quite different morphology. Fig. 2(d) shows the SEM micrograph of solid state reaction derived $\text{CaAl}_2\text{O}_4:\text{Dy}^{3+}$ (5.0 mol%) at 1350°C for 10 h. As shown in Fig. 2(d), $\text{CaAl}_2\text{O}_4:\text{Dy}^{3+}$ phosphors are in the form of irregular blocks without any porous channels. The dimension of the blocks is as large as $10\ \mu\text{m}$ in diameter. A comparison of the micrographs reveals that the sol-gel combustion derived $\text{CaAl}_2\text{O}_4:\text{Dy}^{3+}$ has large surface area, which in turn renders the phosphor rich in oxygen vacancies and abundant in traps for



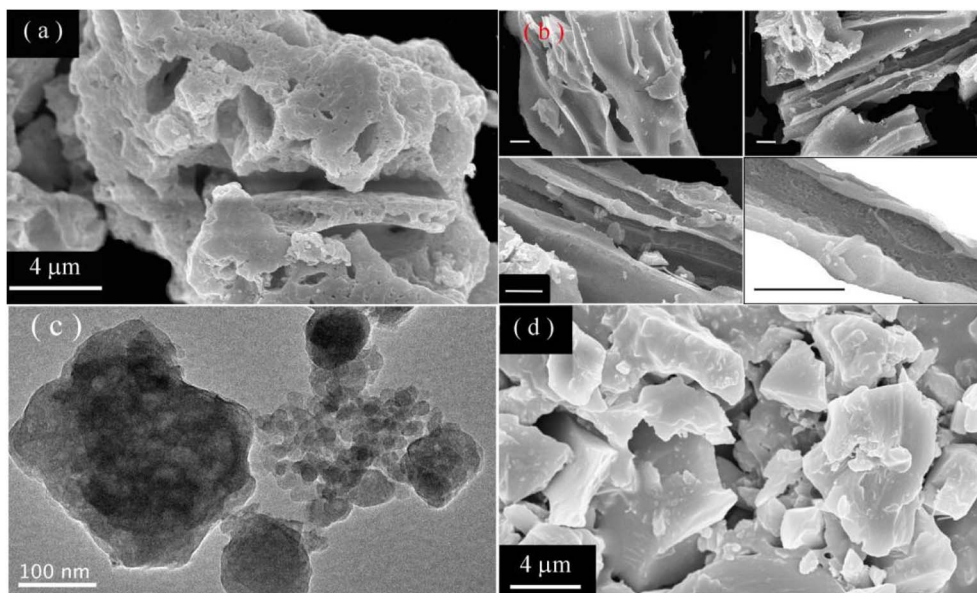


Fig. 2 (a) SEM micrograph of sol-gel combustion derived $\text{CaAl}_2\text{O}_4:\text{Dy}^{3+}$ to show aggregates; (b) SEM micrographs of sol-gel combustion derived $\text{CaAl}_2\text{O}_4:\text{Dy}^{3+}$ to display the channels formed in the aggregates, each scale bar represents 2 μm ; (c) TEM micrograph of sol-gel combustion derived $\text{CaAl}_2\text{O}_4:\text{Dy}^{3+}$ display the nanocrystals formed in the aggregates; (d) SEM micrograph of solid state reaction derived $\text{CaAl}_2\text{O}_4:\text{Dy}^{3+}$ (5.0 mol%) at 1350 $^\circ\text{C}$ for 10 h.

charged carriers. Till date, several rare earth doped CaAl_2O_4 materials are studied and available in literature. For example, Liu *et al.* prepared $\text{CaAl}_2\text{O}_4:\text{Dy}^{3+}$ *via* solid state reaction at 1350 $^\circ\text{C}$.⁶ Due to the features of solid state reaction, the solid state reaction derived $\text{CaAl}_2\text{O}_4:\text{Dy}^{3+}$ phosphors are different from the sol-gel combustion derived ones in the aspects of population density of intrinsic defects. Especially in the sol-gel combustion method, addition of H_3BO_3 lowers reaction temperature, accelerates a diffusion of raw materials, and eventually influences the afterglow properties. Detailed discussions are given by Takeuchi and Kishine in the case of Eu^{2+} and Dy^{3+} codoped SrAl_2O_4 .²²

3.2 EDX spectrum of $\text{CaAl}_2\text{O}_4:\text{Dy}^{3+}$

Fig. 3 depicts the EDX spectrum of sol-gel combustion derived $\text{CaAl}_2\text{O}_4:\text{Dy}^{3+}$ (5.0 mol%). As can be seen in Fig. 3, the characteristic X-ray emissions of $\text{O}(\text{K}\alpha)$, $\text{Al}(\text{K}\alpha)$ and $\text{Ca}(\text{K}\alpha_2)$, and $\text{Ca}(\text{K}\beta_{1,3})$ are located at 0.525, 1.486, 3.693, and 4.013 keV, respectively. Moreover, the characteristic emissions of $\text{Dy}(\text{L}\alpha_1)$ and $\text{Dy}(\text{L}\beta_1)$ can be identified in the EDX spectrum at 6.495 and 7.248 keV, respectively. The X-ray emissions of $\text{Au}(\text{M}\alpha_1)$ at 2.122 keV and $\text{Au}(\text{L}\alpha_1)$ at 9.713 keV are due to Au sputtering for the convenience of SEM characterization. Apparently, the EDX spectrum of $\text{CaAl}_2\text{O}_4:\text{Dy}^{3+}$ confirms the presence of elements Ca, Al, O and Dy in the sample.

3.3 XPS spectrum of $\text{CaAl}_2\text{O}_4:\text{Dy}^{3+}$

The oxidation states of chemical elements in $\text{CaAl}_2\text{O}_4:\text{Dy}^{3+}$ are investigated with the XPS. Fig. 4 represents the XPS survey scan (a) and high-resolution XPS spectra of Ca 2p (b), Al 2p (c), O 1s (d), Dy 3d (e), and Dy 4d (f) in sol-gel combustion derived $\text{CaAl}_2\text{O}_4:\text{Dy}^{3+}$. The nominal doping concentration of Dy^{3+} is 2.0 mol%. As can be seen in Fig. 4(b–d), the binding energies of Ca 2p_{3/2}, Ca 2p_{1/2}, Al 2p_{1/2}, and O 1s are located at approximately 347.3, 350.9, 74.1, and 531.8 eV, respectively. Fig. 4(e) shows that the binding energies of Dy 3d_{5/2} and Dy 3d_{3/2} are located at around 1297.6 and 1335.1 eV, respectively. Fig. 4(f) shows that the binding energies of Dy 4d_{5/2} and Dy 4d_{3/2} are located at around 154.0 and 157.3 eV, respectively. The data in Fig. 4 point out the presence of Ca, Al, O and Dy^{3+} in the phosphor.

3.4 PL excitation spectrum of $\text{CaAl}_2\text{O}_4:\text{Dy}^{3+}$

Fig. 5 shows the PL excitation spectrum of sol-gel combustion derived $\text{CaAl}_2\text{O}_4:\text{Dy}^{3+}$ (2.0 mol%). The emission wavelength is

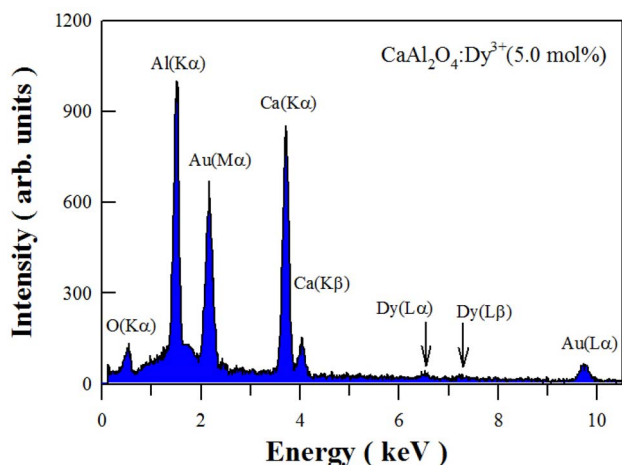


Fig. 3 EDX spectrum of sol-gel combustion derived $\text{CaAl}_2\text{O}_4:\text{Dy}^{3+}$ (5.0 mol%).



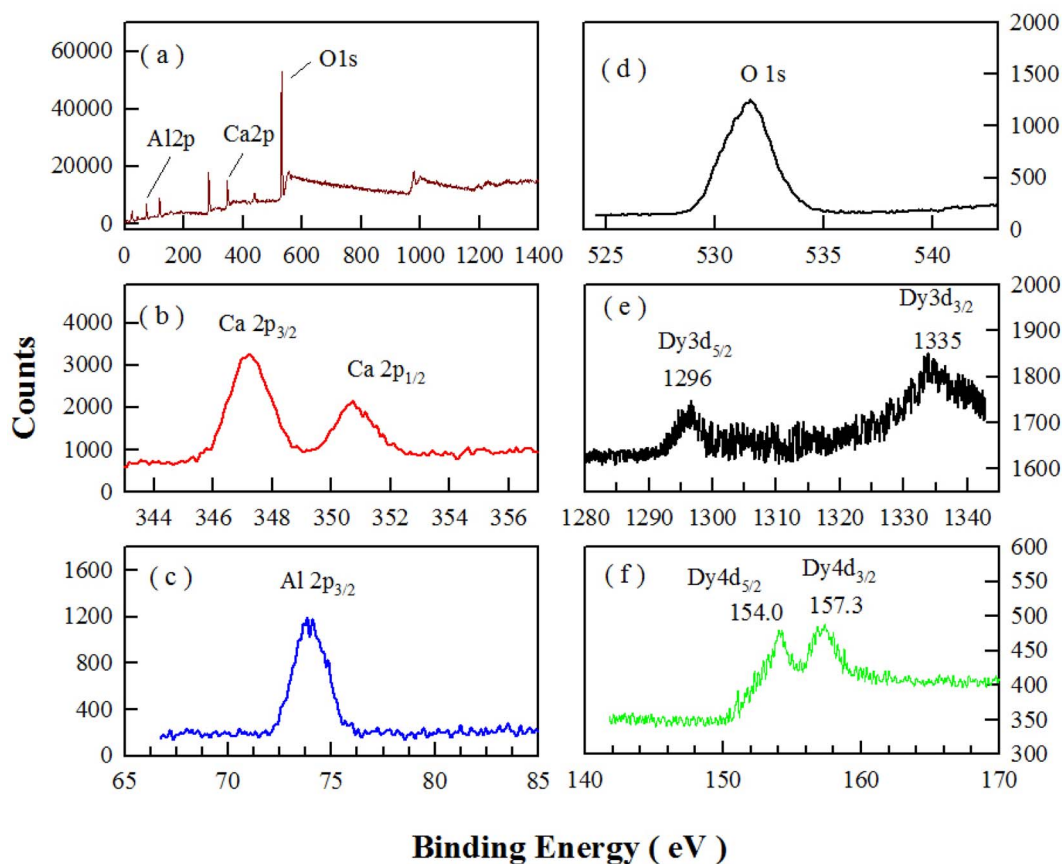


Fig. 4 XPS survey scan (a) and high-resolution XPS spectra of Ca 2p (b), Al 2p (c), O 1s (d), Dy 3d (e), and Dy 4d (f) in sol-gel combustion derived $\text{CaAl}_2\text{O}_4:\text{Dy}^{3+}$ (2.0 mol%).

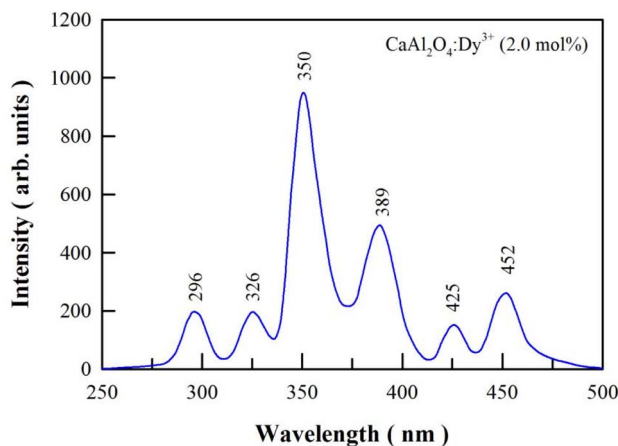


Fig. 5 PL excitation spectrum of sol-gel combustion derived $\text{CaAl}_2\text{O}_4:\text{Dy}^{3+}$ (2.0 mol%). The emission wavelength is fixed at 574 nm.

fixed at 574 nm for the PL excitation measurement. As can be seen in Fig. 5, there are 6 peaks in the PL excitation spectrum of $\text{CaAl}_2\text{O}_4:\text{Dy}^{3+}$ (2.0 mol%), which are located at 296, 326, 350, 389, 425, and 452 nm, respectively. The excitation peaks can be assigned to the 4f-4f transitions of Dy^{3+} .²³⁻²⁵ The strongest absorption of $\text{CaAl}_2\text{O}_4:\text{Dy}^{3+}$ is located at 350 nm, which is due to the ${}^6\text{H}_{15/2} \rightarrow {}^6\text{P}_{7/2}$ transition of Dy^{3+} activator. When compared

to the strongest absorption at 350 nm, $\text{CaAl}_2\text{O}_4:\text{Dy}^{3+}$ exhibits weaker absorptions at 296, 326, 389, 425 and 452 nm. These absorptions are due to ${}^6\text{H}_{15/2} \rightarrow {}^4\text{D}_{7/2}$, ${}^6\text{H}_{15/2} \rightarrow {}^6\text{P}_{3/2}$, ${}^6\text{H}_{15/2} \rightarrow {}^4\text{I}_{13/2}$, ${}^6\text{H}_{15/2} \rightarrow {}^4\text{G}_{11/2}$ and ${}^6\text{H}_{15/2} \rightarrow {}^4\text{I}_{15/2}$ transitions of Dy^{3+} , respectively.²⁶⁻³¹ The PL excitation spectrum indicates that a light source with the emission wavelength of 350 nm excites $\text{CaAl}_2\text{O}_4:\text{Dy}^{3+}$ most efficiently. As a contrast, a light source with the emission wavelength of 326 nm can excite $\text{CaAl}_2\text{O}_4:\text{Dy}^{3+}$ but in a much less efficient manner.

3.5 PL spectra of $\text{CaAl}_2\text{O}_4:\text{Dy}^{3+}$ at different doping concentrations

Fig. 6 represents the PL spectra of sol-gel combustion derived $\text{CaAl}_2\text{O}_4:\text{Dy}^{3+}$ with doping concentrations in the range of 0.1–5.0 mol%. When the doping concentration is as low as 0.1 mol%, the PL spectrum of $\text{CaAl}_2\text{O}_4:\text{Dy}^{3+}$ consists of a broad PL band peaking at about 400 nm whereas the characteristic emissions of Dy^{3+} are hardly discernible, as shown by the PL spectrum (a). The broadband emissions can be attributed to the intrinsic defect emissions in CaAl_2O_4 , which are namely the oxygen and calcium vacancies.^{3,4} The PL properties of undoped CaAl_2O_4 and their origins were discussed in details in our previous work.^{15,16} Actually, similar broadband emissions are recorded for undoped CaAl_2O_4 ,^{15,16} Tb^{3+} doped CaAl_2O_4 ,^{3,4}



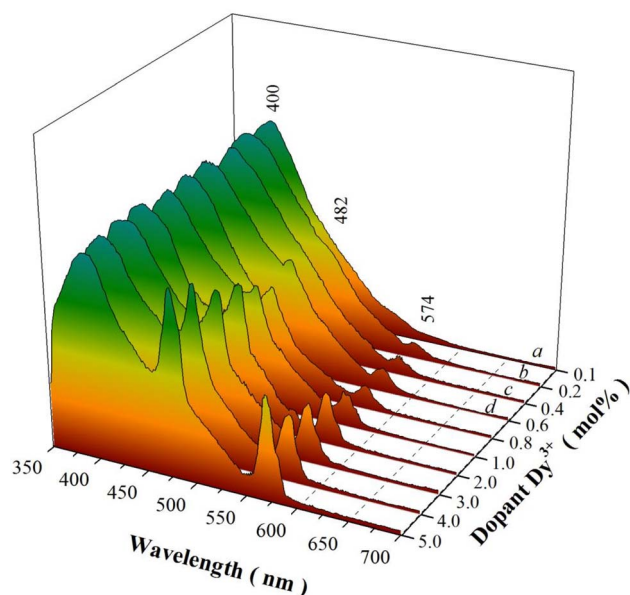
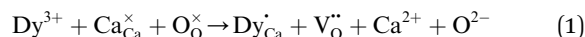


Fig. 6 PL spectra of sol-gel combustion derived $\text{CaAl}_2\text{O}_4:\text{Dy}^{3+}$ with doping concentrations in the range of 0.1–5.0 mol%. Excitation wavelength: 325 nm.

undoped SrAl_2O_4 ,⁸ and Dy^{3+} doped BaAl_2O_4 .²⁰ The characteristic emissions of Dy^{3+} activator are represented by two narrowband emissions peaking at around 482 and 574 nm, respectively, which are due to the ${}^4\text{F}_{9/2} \rightarrow {}^6\text{H}_{15/2}$ and the ${}^4\text{F}_{9/2} \rightarrow {}^6\text{H}_{13/2}$ transitions of Dy^{3+} activator.^{2–4,6,23} As documented in the literature, the transition ${}^4\text{F}_{9/2} \rightarrow {}^6\text{H}_{15/2}$ ($\Delta L = 2$ and $\Delta J = 3$) is magnetic dipole allowed whereas the transition ${}^4\text{F}_{9/2} \rightarrow {}^6\text{H}_{13/2}$ is identified as a hypersensitive electric dipole transition ($\Delta L = 2$ and $\Delta J = 2$) of Dy^{3+} . The reason why the characteristic emissions of Dy^{3+} activator are hardly discernible in the PL spectrum of $\text{CaAl}_2\text{O}_4:\text{Dy}^{3+}$ (0.1 mol%) rests on the fact that the characteristic emissions of Dy^{3+} are too weak when compared to the strong emissions from the intrinsic defects in the host. As the doping concentration is increased to 0.2 and 0.4 mol%, the narrowband emissions of Dy^{3+} at 574 nm become discernible in the PL spectra of $\text{CaAl}_2\text{O}_4:\text{Dy}^{3+}$ (0.2 and 0.4 mol%), as shown by the PL spectra (b) and (c). As the doping concentration is elevated further to 0.6 mol%, the narrowband emissions of Dy^{3+} can be identified clearly in the PL spectrum of $\text{CaAl}_2\text{O}_4:\text{Dy}^{3+}$, as shown by the PL spectrum (d). It is apparent in Fig. 6 that the intensity of the characteristic emissions of Dy^{3+} increases monotonically with the doping concentration. Consequently, the PL spectrum of $\text{CaAl}_2\text{O}_4:\text{Dy}^{3+}$ indicates that the intrinsic defects in CaAl_2O_4 and the doping species Dy^{3+} act as two independent sets of luminescence center of PL in $\text{CaAl}_2\text{O}_4:\text{Dy}^{3+}$. The insight reason for the change in the PL intensity with doping of Dy^{3+} is due to the changes in the population density of the luminescence center of PL. The substitution of Dy^{3+} for Ca^{2+} in the lattice of CaAl_2O_4 promotes the production of two kinds of luminescence center of PL, as shown in eqn (1). The first kind of luminescence center of PL is the Dy^{3+} in Ca^{2+} site while the second kind of luminescence center of PL is the oxygen vacancy.

As the doping concentration of Dy^{3+} increases, the population densities of the two kinds of luminescence center of PL are increased, which in turn lead to the enhancement in the PL intensities. It is noted that the PL intensity of each spectrum in Fig. 6 is normalized at 400 nm.



To check the influences of excitation wavelength on the emissions of $\text{CaAl}_2\text{O}_4:\text{Dy}^{3+}$, we measured the PL spectra of $\text{CaAl}_2\text{O}_4:\text{Dy}^{3+}$ (5 mol%) under different excitation wavelengths. The emission spectra of $\text{CaAl}_2\text{O}_4:\text{Dy}^{3+}$ under the excitations of 326 nm and 350 nm are shown in Fig. S3.† As can be seen in Fig. S3,† the structures of the two PL spectra are nearly identical to each other regardless the variation in the excitation wavelength. However, the emission intensity of $\text{CaAl}_2\text{O}_4:\text{Dy}^{3+}$ (5 mol%) is apparently sensitive to the excitation wavelength. For example, the characteristic emissions of Dy^{3+} are stronger under the excitation of 350 nm than those under the excitation of 326 nm. One of the reasons rests on the fact that Dy^{3+} exhibits stronger absorption at 350 nm than at 326 nm, as endorsed by Fig. 5.

Due to the combined contributions of defect emissions from the host and the characteristic emissions of the dopant, the color coordinates of the emissions of $\text{CaAl}_2\text{O}_4:\text{Dy}^{3+}$ varies with the doping concentration. Color coordinates of luminescent materials, which can be calculated from their PL spectral data, are important parameters to quantitatively describe the emission color for luminescent materials.^{32,33} The CIE chromaticity coordinates of $\text{CaAl}_2\text{O}_4:\text{Dy}^{3+}$ are given in Table S1† for different doping concentrations. As shown in Table S1,† the chromaticity coordinates of $\text{CaAl}_2\text{O}_4:\text{Dy}^{3+}$ change with the doping concentration. For example, the chromaticity coordinates of $\text{CaAl}_2\text{O}_4:\text{Dy}^{3+}$ (0.1 mol%) are (0.156, 0.094), those of $\text{CaAl}_2\text{O}_4:\text{Dy}^{3+}$ (5.0 mol%) are (0.187, 0.176). The emission photos and the CIE chromaticity diagram of $\text{CaAl}_2\text{O}_4:\text{Dy}^{3+}$ are shown in Fig. S4.† It is clear that the PL color of $\text{CaAl}_2\text{O}_4:\text{Dy}^{3+}$ keeps blue when the doping concentration varies in the range of 0.1–5.0 mol%. As referred to the PL spectrum in Fig. 6, the defect-related emissions (blue) of the host are a major constituent in the PL spectrum whereas the characteristic emissions of Dy^{3+} are a minor constituent. That is the reason why the sol-gel combustion derived $\text{CaAl}_2\text{O}_4:\text{Dy}^{3+}$ exhibits blue colored emission in spite of the variation of the doping concentration in the range of 0.1–5.0 mol%.

The assignment of the broadband emissions in Fig. 6 to intrinsic defects in CaAl_2O_4 gains further support from the PL spectrum of solid state reaction derived $\text{CaAl}_2\text{O}_4:\text{Dy}^{3+}$. The solid state reaction route involves chemical decomposition and reactions at much high temperatures (often from 1000 to 1500 °C) to produce a new solid composition. At such high temperatures, oxygen atoms migrate into the crystal lattice to repair the defects with the result of decreased population density of oxygen vacancies in CaAl_2O_4 . Therefore, the broadband emissions should be weakened if the density of oxygen vacancies in CaAl_2O_4 is reduced at high temperature. Fig. 7 depicts the normalized PL spectra of solid state reaction derived



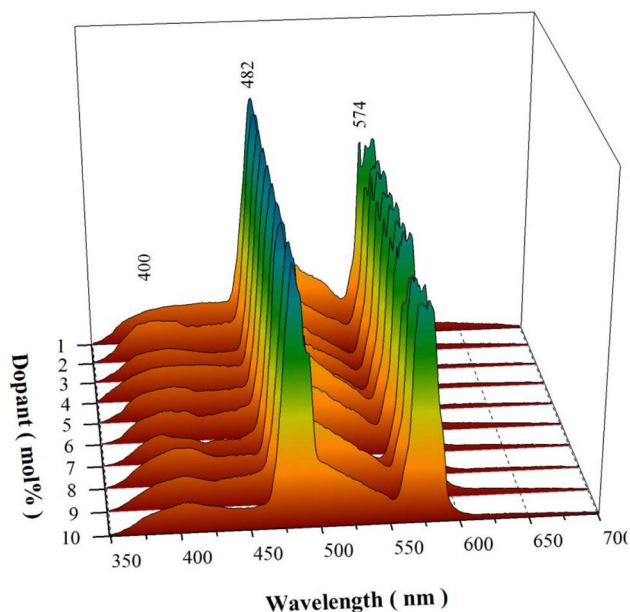


Fig. 7 Normalized PL spectra of solid state reaction derived $\text{CaAl}_2\text{O}_4:\text{Dy}^{3+}$ at $1350\text{ }^\circ\text{C}$ for 10 h.

$\text{CaAl}_2\text{O}_4:\text{Dy}^{3+}$ at $1350\text{ }^\circ\text{C}$ for 10 h. Obviously, each PL spectrum of the solid state reaction derived $\text{CaAl}_2\text{O}_4:\text{Dy}^{3+}$ consists of the characteristic emissions of Dy^{3+} . The most striking feature in Fig. 7 is that the broadband emissions extending from 350 to 450 nm are weakened for the solid state reaction derived $\text{CaAl}_2\text{O}_4:\text{Dy}^{3+}$. The chromaticity coordinates of the solid state reaction derived $\text{CaAl}_2\text{O}_4:\text{Dy}^{3+}$ (10 mol%) are (0.270, 0.365), as shown in Fig. S5.†

3.6 Afterglow spectrum of $\text{CaAl}_2\text{O}_4:\text{Dy}^{3+}$

The emission spectrum of a high-pressure mercury lamp contains a pronounced spectral line at 365.4 nm, which is close to an absorption peak of $\text{CaAl}_2\text{O}_4:\text{Dy}^{3+}$. After exposure to the illumination of a high-pressure mercury lamp (175 W) for 3 min, $\text{CaAl}_2\text{O}_4:\text{Dy}^{3+}$ exhibits intense afterglow after the ultraviolet excitation is blocked off. Fig. S6† depicts the afterglow photos of $\text{CaAl}_2\text{O}_4:\text{Dy}^{3+}$ (0.8 mol%) taken at different times after the irradiation of the high-pressure mercury lamp is blocked off. As shown in Fig. S6,† the white afterglow of $\text{CaAl}_2\text{O}_4:\text{Dy}^{3+}$ (0.8 mol%) can last more than 60 min. The initial luminance of the afterglow is found to depend on the doping concentration of Dy^{3+} . Fig. 8(a) shows the plot of the integrated afterglow intensity of sol-gel combustion derived $\text{CaAl}_2\text{O}_4:\text{Dy}^{3+}$ versus the doping concentration of Dy^{3+} . As can be seen in Fig. 8(a), the optimal doping concentration is around 0.8 mol%. It is noted that the afterglow gets quenched when the doping concentration is high (*i.e.*, 5 mol%). Just like the case of PL quenching at high doping concentration, the non-radiative interaction between dopants is one of the reason of the concentration induced afterglow quenching.³⁴ However, the traps generated by the dopant in the lattice of CaAl_2O_4 should be the key factor to be responsible for the afterglow quenching. As described in eqn

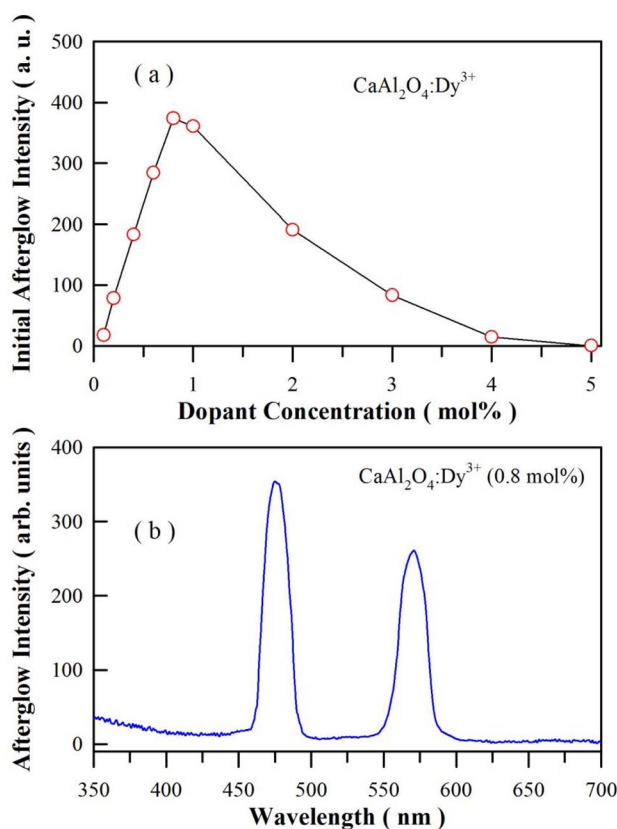


Fig. 8 (a) Plot of the integrated afterglow intensity of sol-gel combustion derived $\text{CaAl}_2\text{O}_4:\text{Dy}^{3+}$ versus the dopant concentration of Dy^{3+} ; (b) afterglow spectrum of sol-gel combustion derived $\text{CaAl}_2\text{O}_4:\text{Dy}^{3+}$ (0.8 mol%) at the doping concentration of 0.8 mol%. Before the afterglow measurement, the phosphor was exposed to the illumination of a high-pressure mercury lamp irradiation (175 W) for 3 min.

(1), doping CaAl_2O_4 with Dy^{3+} results in oxygen vacancies. These positively charged oxygen vacancies can act as electron traps. The increase in the population density as well as the change in the trap depth of these the positively charged oxygen vacancies generate significant effects on the afterglow duration of the phosphor. For example, the afterglow duration is very short when the trap depth is shallow ($E < 0.6\text{ eV}$),^{8,15,16,35} and no afterglow can be observed when the trap depth is too deep ($E > 2.0\text{ eV}$). To observe afterglow at room temperature, the traps should have an appropriate activation energy somewhere between these two extremes, a trap depth around 0.65 eV is considered to be optimal.⁷ Fig. 8(b) depicts the afterglow spectrum of the sol-gel combustion derived $\text{CaAl}_2\text{O}_4:\text{Dy}^{3+}$ at the doping concentration of 0.8 mol%. As can be seen in Fig. 8(b), the afterglow spectrum consists of two narrow emission bands of Dy^{3+} , which is distinctly different from the broadband afterglow of $\text{CaAl}_2\text{O}_4:\text{Eu}^{2+}$.^{1,21,36,37} Thus Fig. 8(b) demonstrates that Dy^{3+} acts as the luminescence center of afterglow for $\text{CaAl}_2\text{O}_4:\text{Dy}^{3+}$. The CIE chromaticity coordinates of the afterglow of $\text{CaAl}_2\text{O}_4:\text{Dy}^{3+}$ (0.8 mol%) are calculated to be (0.265, 0.305), as shown in Fig. S7.† It is clear that the afterglow color of $\text{CaAl}_2\text{O}_4:\text{Dy}^{3+}$ is close to white at the doping level 0.8 mol%. For



comparison, the afterglow spectrum of solid state reaction derived $\text{CaAl}_2\text{O}_4:\text{Dy}^{3+}$ (0.8 mol%) is given in the ESI as Fig. S8.†

3.7 Afterglow decay profile of $\text{CaAl}_2\text{O}_4:\text{Dy}^{3+}$

The duration of afterglow is a straightforward and standardized parameter to evaluate the properties of an afterglow material, whereby 0.32 mcd m^{-2} is often used as threshold for defining the duration of an afterglow. Fig. 9 depicts the afterglow decay profile of sol-gel combustion derived $\text{CaAl}_2\text{O}_4:\text{Dy}^{3+}$ (0.8 mol%). The phosphor was exposed to illumination of a high-pressure mercury lamp irradiation (175 W) for 3 min before the measurement of afterglow decay curve. As shown by the raw data in Fig. 9, the afterglow duration of $\text{CaAl}_2\text{O}_4:\text{Dy}^{3+}$ is determined to be about 115 min. It is found that the decay curves in Fig. 9 could be best fitted to the tri-exponential function according to eqn (2)

$$I(t) = I_1 \exp(-t/\tau_1) + I_2 \exp(-t/\tau_2) + I_3 \exp(-t/\tau_3), \quad (2)$$

where $I(t)$ is the afterglow intensity at time t after blocking the laser excitation, I_i is the prefactor of the exponential component whose lifetime decay constant is τ_i ($i = 1-3$). The red solid line in Fig. 9 represents the fit of the experimental signals by eqn (2). The fitting parameters are tabulated in the figure. Clearly, the $\text{CaAl}_2\text{O}_4:\text{Dy}^{3+}$ has three largely different decay components with constants of $\tau_1 = 2.51 \text{ min}$, $\tau_2 = 11.31 \text{ min}$ and $\tau_3 = 89.29 \text{ min}$. We can see that τ_2 and τ_3 are much longer than τ_1 , suggesting the presence of deeper traps in the phosphor. The luminance reading of the first data point in Fig. 9 is 8.3 mcd m^{-2} at 3.67 min . In order to derive the luminance at $t = 0$, it is necessary to extrapolate the data, yielding the value of the luminance to be 22.35 mcd m^{-2} at $t = 0$. It is worth of noting that the luminance of the phosphor at the initial moment is different from the luminance of the first component at the initial moment (*i.e.*, $I_1 = 16.56 \text{ mcd m}^{-2}$). Actually, the luminance of the phosphor at the initial moment is the summation of the luminance of the three components at the initial

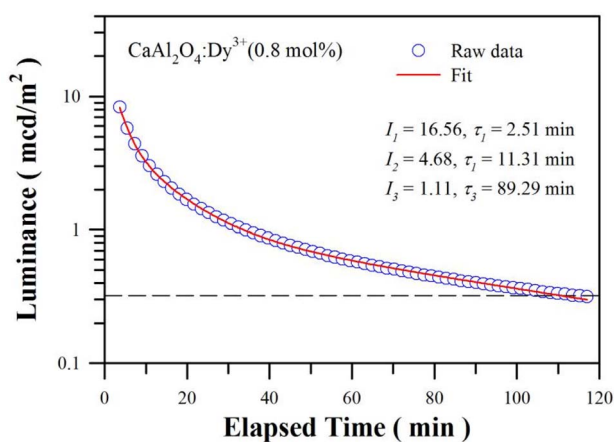


Fig. 9 Afterglow decay profile of sol-gel combustion derived $\text{CaAl}_2\text{O}_4:\text{Dy}^{3+}$ (0.8 mol%). The dash line represents the threshold luminance of 0.32 mcd m^{-2} .

moment, that is, the sum of I_1 , I_2 and I_3 . Moreover, the afterglow duration of the phosphor is different from the longest lifetime decay constant τ_3 (*i.e.*, 89.29 min). According to eqn (1), the afterglow duration of the phosphor is defined by the variable t when $I(t)$ reaches the threshold 0.32 mcd m^{-2} . The luminance decreases to $0.3205 \text{ mcd m}^{-2}$ when $t = 111 \text{ min}$. Consequently, the afterglow duration derived from eqn (2) (about 111 min) is very close the afterglow duration derived from raw data (about 115 min).

Being distinctly different from PL decay, the afterglow phenomenon is a particular case of thermostimulated luminescence and is a defect dependent phenomenon.^{7,38} Additional notes can be found in the ESI.† The afterglow duration of $\text{CaAl}_2\text{O}_4:\text{Dy}^{3+}$ heavily depends on the wavelength of ultraviolet excitation. The afterglow of $\text{CaAl}_2\text{O}_4:\text{Dy}^{3+}$ (0.8 mol%) lasts for about 60 s when the 325 nm excitation of the He-Cd laser (13 mW) is switched off. Conversely, the afterglow of $\text{CaAl}_2\text{O}_4:\text{Dy}^{3+}$ (0.8 mol%) lasts for only 30 s when the 254 nm irradiation of a low-pressure mercury lamp (32 W) is turned off. Moreover, the afterglow duration of $\text{CaAl}_2\text{O}_4:\text{Dy}^{3+}$ depends on the doping concentration when the wavelength of ultraviolet excitation is fixed. For example, after exposed to the 254 nm irradiation of a low-pressure mercury lamp (32 W) for 5 min, the afterglows of $\text{CaAl}_2\text{O}_4:\text{Dy}^{3+}$ last for about 5, 8, 14, 19, 30, 60, 120, 75, 10 and 0 s when the doping concentrations are 0.1, 0.2, 0.4, 0.6, 0.8, 1.0, 2.0, 3.0, 4.0 and 5.0 mol%, respectively.

3.8 Possible PL and afterglow mechanisms of $\text{CaAl}_2\text{O}_4:\text{Dy}^{3+}$

CaAl_2O_4 is an insulator with a bandgap of around 6.7 eV.^{39,40} Oxygen and calcium vacancies are intrinsic defects in $\text{CaAl}_2\text{O}_4:\text{Dy}^{3+}$. On one hand, these intrinsic vacancies act as luminescence center of PL with the result of a broadband PL spectrum peaking at about 400 nm.^{15,16} On the other hand, these intrinsic vacancies work as traps for charged carriers. For example, oxygen vacancies in CaAl_2O_4 are proposed to work as electron traps because they are positively charged whereas calcium vacancies are potential hole traps because they are positively charged.^{10,39} Dopant Dy^{3+} belongs to extrinsic defect in $\text{CaAl}_2\text{O}_4:\text{Dy}^{3+}$. After Dy^{3+} ions are incorporated into the host, a series of defect energy levels are introduced into the bandgap of CaAl_2O_4 . The lowest energy level of the excited state of Dy^{3+} is known as ${}^4\text{F}_{9/2}$ while the energy levels of the ground state of Dy^{3+} are denoted as ${}^6\text{H}_j$ ($j = 15/2-5/2$). As evidenced by the characteristic emissions in Fig. 6, 7 and S3,† dopant Dy^{3+} ions act as luminescent center of PL in $\text{CaAl}_2\text{O}_4:\text{Dy}^{3+}$ to yield narrowband emissions peaking at 482 and 574 nm, respectively. Furthermore, this extrinsic defect can work as electron trap because it is positively charged.

Fig. 10 schematically illustrates the PL and afterglow mechanisms of $\text{CaAl}_2\text{O}_4:\text{Dy}^{3+}$. The energy levels of oxygen vacancies and dopant Dy^{3+} are depicted in the bandgap of CaAl_2O_4 . As shown in Fig. 10, oxygen vacancies and Dy^{3+} activator are two independent sets of photon absorbents in $\text{CaAl}_2\text{O}_4:\text{Dy}^{3+}$. Upon the ultraviolet excitation at 325 nm (3.82 eV), a portion of the incident photons are absorbed by the host due to the presence of a large number of oxygen vacancies in CaAl_2O_4 (process ①).



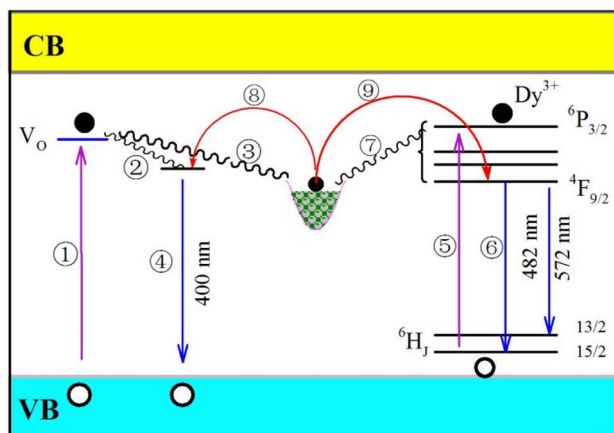


Fig. 10 Schematic illustration on the PL and afterglow mechanisms of $\text{CaAl}_2\text{O}_4:\text{Dy}^{3+}$. Process ①: host absorption of incident photons due to the presence of intrinsic defects in CaAl_2O_4 . Process ②: non-radiative relaxation of hot electrons to oxygen vacancies (luminescence center) in CaAl_2O_4 . Process ③: non-radiative relaxation of hot electrons to electron traps in CaAl_2O_4 . Process ④: radiative recombination of electrons captured at oxygen vacancy with holes in the valence band to yield the broadband emissions peaking at about 400 nm. Process ⑤: absorption of incident photons due to the transition ${}^6\text{H}_{15/2} \rightarrow {}^6\text{P}_{3/2}$ of Dy^{3+} (around 325 nm) in CaAl_2O_4 . Process ⑥: electron transitions ${}^4\text{F}_{9/2} \rightarrow {}^6\text{H}_{15/2}$ and ${}^4\text{F}_{9/2} \rightarrow {}^6\text{H}_{13/2}$ of Dy^{3+} to produce the characteristic emissions of Dy^{3+} . Process ⑦: non-radiative relaxation of hot electrons at excited states of Dy^{3+} to electron traps in CaAl_2O_4 . Process ⑧: thermal release of electrons from electron traps to oxygen vacancies in CaAl_2O_4 . Process ⑨: thermal release of electrons from electron traps to the excited states of Dy^{3+} .

After non-radiative relaxations, the hot electrons are captured by either the oxygen vacancies (process ②) or the electron traps (process ③). The subsequent radiative recombination of electrons captured at oxygen vacancies with holes in the valence band of CaAl_2O_4 yields the broadband PL peaking at about 400 nm (process ④). Since the transition ${}^6\text{H}_{15/2} \rightarrow {}^6\text{P}_{3/2}$ of Dy^{3+} (326 nm) matches well with the 325 nm excitation of the laser, some incident photons are absorbed by Dy^{3+} activator in CaAl_2O_4 (process ⑤). It is noted that several energy levels are located between the excited state ${}^6\text{P}_{3/2}$ and the lowest excited state ${}^6\text{H}_{15/2}$, among which include ${}^4\text{I}_{13/2}$, ${}^4\text{P}_{5/2}$ and ${}^6\text{P}_{7/2}$. With the assistance of phonons, a portion of hot electrons at the excited state ${}^6\text{P}_{3/2}$ are relaxed to the lowest excited state ${}^4\text{F}_{9/2}$. Then electron transitions ${}^4\text{F}_{9/2} \rightarrow {}^6\text{H}_{15/2}$ and ${}^4\text{F}_{9/2} \rightarrow {}^6\text{H}_{13/2}$ of Dy^{3+} lead to the characteristic emissions of Dy^{3+} (process ⑥). Apart from the radiation recombination, some hot electrons at excited states of Dy^{3+} can be captured by the electron traps *via* non-radiative relaxations (process ⑦). In the light of the proposed mechanisms in Fig. 10, the PL features of $\text{CaAl}_2\text{O}_4:\text{Dy}^{3+}$ can be interpreted: (i) the PL spectrum of $\text{CaAl}_2\text{O}_4:\text{Dy}^{3+}$ consists of one broadband and two characteristic emissions of Dy^{3+} ; and (ii) the characteristic emissions of Dy^{3+} becomes dominant over the broadband emissions when the population density of oxygen vacancies in $\text{CaAl}_2\text{O}_4:\text{Dy}^{3+}$ is significantly suppressed *via* the solid state reaction at high temperatures.

Once the ultraviolet excitation is ceased, processes ①–⑦ are stopped immediately. Under thermal activation, electrons can be released from the electron traps *via* processes ⑧ and ⑨. Subsequently, afterglow with characteristic emissions of Dy^{3+} is resulted when the electrons released from the excited states of Dy^{3+} recombine radiatively with holes *via* process ⑥. Theoretically speaking, afterglow with broadband emissions peaking at about 400 nm should be observed when thermally detrapped electrons recombine radiatively with holes *via* process ④. In practice, such a broadband afterglow is negligible because its intensity is several orders of magnitude weaker than that of Dy^{3+} related afterglows. Therefore, the afterglow spectrum of the $\text{CaAl}_2\text{O}_4:\text{Dy}^{3+}$ consists of two narrowband emissions peaking at 482 and 574 nm, respectively.

In the light of the PL and afterglow mechanisms of $\text{CaAl}_2\text{O}_4:\text{Dy}^{3+}$ in Fig. 10, electrons in the electron traps contribute to the PL under photoexcitation, too. Upon the photoexcitation, some electrons in the electron traps are detrapped *via* processes ⑧ and ⑨. Broadband emissions peaking at around 400 nm can be expected when the detrapped electrons recombine radiatively with holes *via* the radiative process ④, and narrowband emissions of Dy^{3+} can be resulted when the detrapped electrons recombine radiatively with holes *via* the radiative process ⑥. In most cases, however, such contributions are negligible because they are many times weaker than the emissions resulted directly from the ultraviolet photoexcitation. Only when the afterglow is sufficiently strong, such contributions to the PL are discernible. For example, the PL spectrum of Dy^{3+} doped SrAl_2O_4 is the result of superposition of the broadband emissions of the host peaking at about 400 nm and another broadband emissions peaking at about 520 nm.^{12,13}

3.9 TL glow curves of $\text{CaAl}_2\text{O}_4:\text{Dy}^{3+}$

TL is an important tool to determine the activation energies (*i.e.*, trap depths) of trapping levels in crystals.^{37,39,41,42} Fig. 11 represents the TL glow curves of sol-gel combustion derived $\text{CaAl}_2\text{O}_4:\text{Dy}^{3+}$ with different doping concentrations. Each $\text{CaAl}_2\text{O}_4:\text{Dy}^{3+}$ phosphor was exposed to ultraviolet light of 254 nm for 5 min before the TL measurements. The temperature rising rate was 2 K min^{-1} . It can be seen that each TL glow curve in Fig. 11 exhibits an extremely broad and asymmetric profile, suggesting the presence of multiple trap levels in $\text{CaAl}_2\text{O}_4:\text{Dy}^{3+}$.⁴³ Moreover, both the profile and the peak temperature of the TL glow curve are sensitive to the doping concentration: (i) the TL glow curve consists of a primary peak at around 350 K and a secondary peak at about 310 K when the doping concentration increases from 0.1 to 0.4 mol%; (ii) the TL glow curve has only one peak, which gradually shifts to higher temperature (from 350 to 375 K) as the doping concentration increases from 0.6 to 0.8 mol%; and (iii) the TL glow curve has only one peak, which gradually shifts to lower temperature (from 375 to 350 K) as the doping concentration increases further from 1.0 to 5.0 mol%. The vertical dash line in Fig. 11 marks the position of 350 K. With the vertical line as a guideline, the evolution of the peak temperature with the doping concentration can be identified clearly. Interestingly, the peak



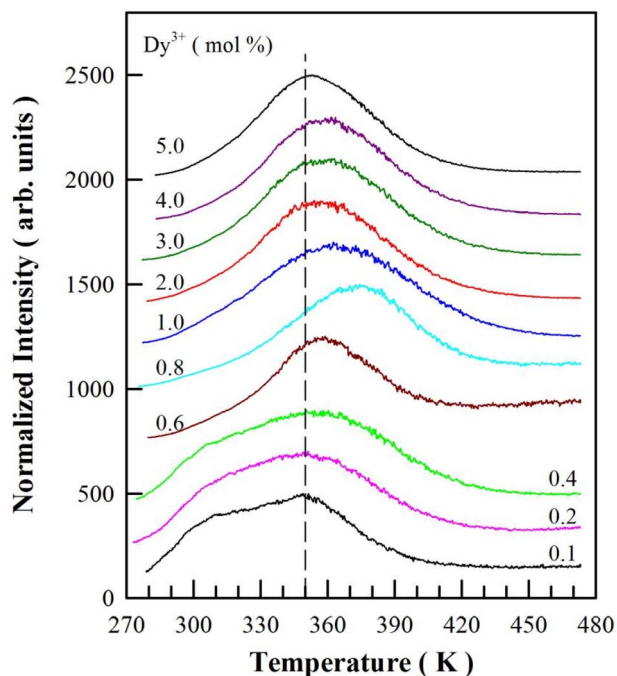


Fig. 11 TL glow curves of sol-gel combustion derived $\text{CaAl}_2\text{O}_4:\text{Dy}^{3+}$ with different doping concentrations. $\text{CaAl}_2\text{O}_4:\text{Dy}^{3+}$ phosphors were exposed to ultraviolet light of 254 nm for 5 min before the TL measurement.

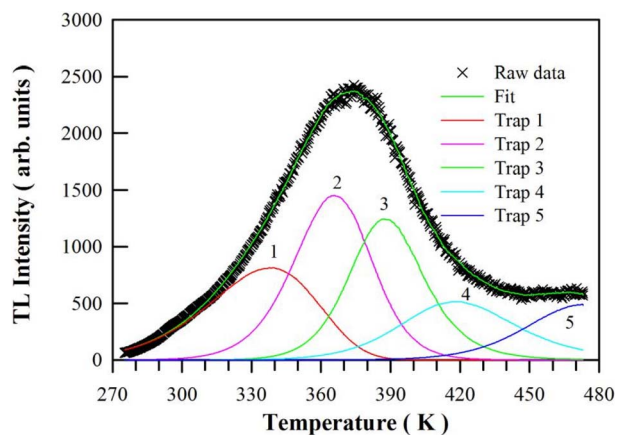


Fig. 12 Computerized glow curve deconvolution of the TL glow curve of $\text{CaAl}_2\text{O}_4:\text{Dy}^{3+}$ (0.8 mol%) under the assumption of 5 traps in the phosphor.

temperature of the TL glow curve of $\text{CaAl}_2\text{O}_4:\text{Dy}^{3+}$ (0.8 mol%) is the highest (around 375 K) among the 10 phosphors under test, which coincides with the best afterglow performance of $\text{CaAl}_2\text{O}_4:\text{Dy}^{3+}$ at optimal doping concentration of 0.8 mol%.

To understand the TL behavior of $\text{CaAl}_2\text{O}_4:\text{Dy}^{3+}$, it is necessary to deconvolute each TL glow curve and evaluate the trapping parameters. The TL curve based on the general order function is given by the following equation:

$$I(T) = sn_0 \exp\left(-\frac{E}{kT}\right) \times \left[1 + \left(\frac{b-1}{\beta}\right)s \times \int_{T_0}^T \exp\left(-\frac{E}{kT'}\right) dT'\right]^{-b/(b-1)}, \quad (3)$$

where I is the TL intensity at temperature T , s is the pre-exponential factor with the unit of s^{-1} , n_0 is the concentration of trapped charges at time $t = 0$, E is the trap depth, k is the Boltzmann constant, b is the order of kinetics, and β is the heating rate. In order to determine the kinetic parameters of the multiple traps, computerized glow curve deconvolution of the TL glow curves is carried out with general order kinetics using a computer program given by Chung *et al.*⁴⁴ Fig. 12 depicts the computerized glow curve deconvolution of the TL glow curve of $\text{CaAl}_2\text{O}_4:\text{Dy}^{3+}$ at the doping concentration of 0.8 mol%. It is found that this TL glow curve can be described satisfactorily by using the general order kinetics to model 5 traps in $\text{CaAl}_2\text{O}_4:\text{Dy}^{3+}$. The figure-of-merit (FOM) of the deconvolution is 2.071%. The kinetic parameters and the electron lifetime at room temperature (τ_{300}) are summarized in Table 1 for each trap in the $\text{CaAl}_2\text{O}_4:\text{Dy}^{3+}$ (0.8 mol%). As can be seen in Table 1, the calculated E values are 0.3919, 0.8219, 1.1466, 0.8403 and 1.0352 eV for the five traps in $\text{CaAl}_2\text{O}_4:\text{Dy}^{3+}$ (0.8 mol%). Apparently, most of these traps are suitable for long-time afterglow.

In addition to the TL glow curve shown in Fig. 12, we have also deconvoluted the TL glow curves of $\text{CaAl}_2\text{O}_4:\text{Dy}^{3+}$ with the doping concentrations of 0.1, 0.2, 0.4, 0.6, 1.0, 2.0, 3.0, 4.0 and 5.0 mol%, respectively. For the sake of brevity, the computerized glow curve deconvolutions of the TL glow curves of $\text{CaAl}_2\text{O}_4:\text{Dy}^{3+}$ are shown in ESI as Fig. S9–S17.† The kinetic parameters and the electron lifetime at room temperature are listed in Table S2† for each trap in the $\text{CaAl}_2\text{O}_4:\text{Dy}^{3+}$. Apparently, the parameters of electron traps in $\text{CaAl}_2\text{O}_4:\text{Dy}^{3+}$ can be effectively tuned *via* the control of doping concentration, which in turn can be exploited to modify the brightness and duration of the afterglow of $\text{CaAl}_2\text{O}_4:\text{Dy}^{3+}$.

Table 1 Kinetic parameters of the computerized glow curve deconvolution of the TL glow curve of $\text{CaAl}_2\text{O}_4:\text{Dy}^{3+}$ (0.8 mol%). T_m represents the peak temperature, E is the trap-depth, s is the frequency factor, b is the order of kinetics, and τ_{300} is the room temperature electron lifetime in the trap

Trap number	T_m (K)	E (eV)	s (s^{-1})	b	τ_{300} (h)	FOM (%)
1	339.25	0.3919	9.234×10^2	1.000	1.93×10^0	2.071
2	365.55	0.8219	4.810×10^8	1.482	2.11×10^2	
3	386.45	1.1466	2.256×10^{12}	2.000	1.02×10^6	
4	418.95	0.8403	2.336×10^7	2.000	4.71×10^5	
5	472.85	1.0352	1.683×10^8	2.000	1.59×10^8	



4. Conclusions

With doping concentration varying in the range of 0.1–5.0 mol%, a series of $\text{CaAl}_2\text{O}_4:\text{Dy}^{3+}$ phosphors have been synthesized *via* sol–gel combustion technique. The PL and afterglow mechanisms of sol–gel combustion derived $\text{CaAl}_2\text{O}_4:\text{Dy}^{3+}$ are explored by means of XRD, SEM, TEM, EDX, XPS, PL, afterglow spectroscopy and TL dosimetry. The PL spectrum of $\text{CaAl}_2\text{O}_4:\text{Dy}^{3+}$, which consists of a broad PL band peaking at about 400 nm and the characteristic emissions of Dy^{3+} , indicates that oxygen vacancies and Dy^{3+} work as two independent sets of luminescence center of PL for $\text{CaAl}_2\text{O}_4:\text{Dy}^{3+}$. As a contrast, the afterglow spectrum of $\text{CaAl}_2\text{O}_4:\text{Dy}^{3+}$ consists of the characteristic emissions of Dy^{3+} only, verifying that dopant Dy^{3+} acts as the luminescence center of afterglow for $\text{CaAl}_2\text{O}_4:\text{Dy}^{3+}$. The afterglow duration of $\text{CaAl}_2\text{O}_4:\text{Dy}^{3+}$ is found to depend on the doping concentration, and 115 min-long afterglow is recorded for $\text{CaAl}_2\text{O}_4:\text{Dy}^{3+}$ at the optimal doping concentration of 0.8 mol%. The profile and peak temperature of the TL glow curve are sensitive to the doping concentration. The TL glow curve of $\text{CaAl}_2\text{O}_4:\text{Dy}^{3+}$ (0.8 mol%) exhibits a maximal peak temperature at around 375 K. A picture on the PL and afterglow mechanisms is given to reveal the processes of excitation, migration, trapping, detrapping, and radiative recombination of charged carriers in $\text{CaAl}_2\text{O}_4:\text{Dy}^{3+}$.

Conflicts of interest

There are no conflicts to declare.

Acknowledgements

Financial support from National Natural Science Foundation of China (no. 11574036) is acknowledged.

References

- P. F. Smet, N. Avci, K. Van den Eeckhout and D. Poelman, Extending the afterglow in CaAl_2O_4 : Eu, Nd persistent phosphors by electron beam annealing, *Opt. Mater. Express*, 2012, **2**, 1306–1313.
- A. H. Wako, B. F. Dejene and H. C. Swart, Roles of doping ions in afterglow properties of blue CaAl_2O_4 : Eu^{2+} , Nd^{3+} phosphors, *Phys. B*, 2014, **439**, 153–159.
- B. G. Zhai, H. Xu and Y. M. Huang, Annealing temperature dependent afterglow of Tb^{3+} doped CaAl_2O_4 , *Opt. Mater.*, 2021, **112**, 110739.
- B. G. Zhai and Y. M. Huang, Extending the afterglow of Tb^{3+} doped CaAl_2O_4 to 8 hours *via* the control of doping concentration, *J. Lumin.*, 2022, **244**, 118725.
- R. Shrivastava, J. Kaur and V. Dubey, White light emission by Dy^{3+} doped phosphor matrices: a short review, *J. Fluoresc.*, 2016, **26**, 105–111.
- B. Liu, C. Shi and Z. Qi, Potential white-light long-lasting phosphor: Dy^{3+} -doped aluminate, *Appl. Phys. Lett.*, 2005, **86**, 191111.
- K. Van den Eeckhout, P. F. Smet and D. Poelman, Persistent luminescence in Eu^{2+} -doped compounds: a review, *Materials*, 2010, **3**, 2536–2566.
- B. G. Zhai and Y. M. Huang, Green afterglow of undoped SrAl_2O_4 , *Nanomaterials*, 2021, **11**, 2331.
- M. Ziyauddin, S. Tigga, N. Brahme and D. P. Bisen, Photoluminescence and thermoluminescence studies of $\text{CaAl}_2\text{O}_4:\text{Dy}^{3+}$ phosphor, *Lumin.*, 2016, **31**, 76–80.
- V. Vitola, D. Millers, I. Bite, K. Smits and A. Spustaka, Recent progress in understanding the persistent luminescence in $\text{SrAl}_2\text{O}_4:\text{Eu}$, Dy, *Mater. Sci. Technol.*, 2019, **35**, 1661–1677.
- Q. L. Ma, B. G. Zhai and Y. M. Huang, Effect of sol–gel combustion temperature on the luminescent properties of trivalent Dy doped SrAl_2O_4 , *Ceram. Int.*, 2015, **41**, 5830–5835.
- Y. M. Huang and Q. L. Ma, Long afterglow of trivalent dysprosium doped strontium aluminate, *J. Lumin.*, 2015, **160**, 271–275.
- B. G. Zhai, L. Yang, Q. L. Ma, X. Liu and Y. M. Huang, Mechanism of the prolongation of the green afterglow of $\text{SrAl}_2\text{O}_4:\text{Dy}^{3+}$ caused by the use of H_3BO_3 flux, *J. Lumin.*, 2017, **181**, 78–87.
- N. Yamashita, T. Hamada, M. Takada, M. Katsuki and M. Nakagawa, Photoluminescence and thermoluminescence of MgSO_4 , CaSO_4 , SrSO_4 and BaSO_4 powder phosphors activated with Tb^{3+} , *Jpn. J. Appl. Phys., Part 1*, 2001, **40**, 6732–6736.
- B. G. Zhai and Y. M. Huang, Blue afterglow from undoped CaAl_2O_4 , *Europhys. Lett.*, 2019, **127**, 17001.
- B. G. Zhai, H. Xu, F. Zhuo and Y. M. Huang, Annealing temperature dependent photoluminescence and afterglow of undoped CaAl_2O_4 , *J. Alloys Compd.*, 2020, **821**, 153563.
- K. A. Gedekar, S. P. Wankhede, S. V. Moharil and R. M. Belekar, d–f luminescence of Ce^{3+} and Eu^{2+} ions in BaAl_2O_4 , SrAl_2O_4 and CaAl_2O_4 phosphors, *J. Adv. Ceram.*, 2017, **6**, 341–350.
- R. D. Shannon, Revised effective ionic radii and systematic studies of interatomic distances in halides and chalcogenides, *Acta Crystallogr., Sect. A: Cryst. Phys., Diffraction, Theor. Gen. Crystallogr.*, 1976, **32**, 751–767.
- B. G. Zhai and Y. M. Huang, Green photoluminescence and afterglow of Tb doped SrAl_2O_4 , *J. Mater. Sci.*, 2017, **52**, 1813–1822.
- B. G. Zhai, Q. L. Ma, R. Xiong, X. Li and Y. M. Huang, Blue-green afterglow of $\text{BaAl}_2\text{O}_4:\text{Dy}^{3+}$ phosphors, *Mater. Res. Bull.*, 2016, **75**, 1–6.
- V. Singh, J.-J. Zhu, M. K. Bhide and V. Natarajan, Synthesis, characterisation and luminescence investigations of Eu activated CaAl_2O_4 phosphor, *Opt. Mater.*, 2007, **30**, 446–450.
- N. Takeuchi and K. Kishine, Effect of addition of boron on the long afterglow property of SrAl_2O_4 : Eu^{2+} , Dy^{3+} phosphor, *Mater. Trans.*, 2021, **62**, 1039–1045.
- R. Shrivastava, J. Kaur and M. Dash, Studies on white light emission of $\text{Sr}_2\text{MgSi}_2\text{O}_7$ doped with Dy^{3+} phosphors, *Superlattices Microstruct.*, 2015, **82**, 262–268.
- P. P. Pawar, S. R. Munishwar and R. S. Gedam, Physical and optical properties of $\text{Dy}^{3+}/\text{Pr}^{3+}$ co-doped lithium borate glasses for W-LED, *J. Alloys Compd.*, 2016, **660**, 347–355.



- 25 X. Chen, T. Lu, Y. Wu, N. Wei, J. Qi, L. Chen and Y. Liu, Ammonium citrate-assisted combustion synthesis and photoluminescence properties of Dy:YAG nanophosphors, *J. Sol-Gel Sci. Technol.*, 2016, **79**, 606–615.
- 26 M. A. Tshabalala, F. B. Dejene, S. S. Pitale, H. C. Swart and O. M. Ntwaeaborwa, Generation of white-light from Dy³⁺ doped Sr₂SiO₄ phosphor, *Phys. B*, 2014, **439**, 126–129.
- 27 Y. Chen, X. Cheng, M. Liu, Z. Qi and C. Shi, Comparison study of the luminescent properties of the white-light long afterglow phosphors: Ca_xMgSi₂O_{5+x}:Dy³⁺ (x = 1,2,3), *J. Lumin.*, 2009, **129**, 531–535.
- 28 S. Cho, Photoluminescence properties of BaMoO₄:RE³⁺ (RE = Eu, Sm, Dy, Tb, Tm) phosphors, *J. Korean Phys. Soc.*, 2016, **69**, 1479–1484.
- 29 A. Balakrishna and O. M. Ntwaeaborwa, Study of luminescent behavior and crystal defects of different MNA [PO₄]-Dy³⁺ phosphors (M = Mg, Ca, Sr and Ba), *Sens. Actuators, B*, 2017, **242**, 305–317.
- 30 B. Shanmugavelu and V. V. Ravi Kanth Kumar, Luminescence studies of Dy³⁺ doped bismuth zinc borate glasses, *J. Lumin.*, 2014, **146**, 358–363.
- 31 S. Xin and G. Zhu, The synthesis and photoluminescence properties investigation of a versatile phosphor Sr₁₀[(PO₄)_{5.5}(BO₄)_{0.5}](BO₂): Sb³⁺/Eu³⁺/Pr³⁺/Dy³⁺, *J. Lumin.*, 2017, **181**, 443–447.
- 32 Q. L. Ma, R. Xiong and Y. M. Huang, Tunable photoluminescence of porous silicon by liquid crystal infiltration, *J. Lumin.*, 2011, **131**, 2053–2057.
- 33 Q. L. Ma, B. G. Zhai and Y. M. Huang, Sol-gel derived ZnO/porous silicon composites for tunable photoluminescence, *J. Sol-Gel Sci. Technol.*, 2012, **64**, 110–116.
- 34 B. G. Zhai and Y. M. Huang, Doping concentration dependent photoluminescence and afterglow of Eu²⁺ doped CaAl₂O₄ for insight into the afterglow mechanisms, *Phys. B*, 2022, **646**, 414284.
- 35 B. G. Zhai, H. Xu, Q. Zhang and Y. M. Huang, Blue photoluminescence and cyan-colored afterglow of undoped SrSO₄ nanoplates, *ACS Omega*, 2021, **6**, 10129–10140.
- 36 T. Aitasalo, J. Holsa, H. Jungner, M. Lastusaari and J. Niittykoski, Comparison of sol-gel and solid-state prepared Eu²⁺ doped calcium aluminates, *Mater. Sci.*, 2002, **20**, 15–20.
- 37 T. Aitasalo, J. Holsa, H. Jungner, M. Lastusaari, J. Niittykoski, M. Parkkinen and R. Valtonen, Eu²⁺ doped calcium aluminates prepared by alternative low temperature routes, *Opt. Mater.*, 2004, **26**, 113–116.
- 38 D. L. Fritzen, L. Giordano, L. C. V. Rodrigues and J. H. S. K. Monteiro, Opportunities for persistent luminescent nanoparticles in luminescence imaging of biological systems and photodynamic therapy, *Nanomaterials*, 2020, **10**, 2015.
- 39 T. Aitasalo, J. Hölsä, H. Jungner, M. Lastusaari and J. Niittykoski, Thermoluminescence study of persistent luminescence materials: Eu²⁺- and R³⁺-doped calcium aluminates, CaAl₂O₄:Eu²⁺, R³⁺, *J. Phys. Chem. B*, 2006, **110**, 4589–4598.
- 40 J. Holsa, T. Laamanen, M. Lastusaari, M. Malkamaki, J. Niittykoski and P. Novák, Synchrotron radiation spectroscopy of rare earth doped persistent luminescence materials, *Radiat. Phys. Chem.*, 2009, **78**, S11–S16.
- 41 R. K. Gartia, M. N. Singh, L. P. Chanu and T. B. Singh, Determination of thermoluminescence parameters in nanocrystalline CaAl₂O₄, *J. Lumin.*, 2020, **219**, 116867.
- 42 M. N. Singh and R. K. Gartia, The physical basis of persistence luminescence in CaAl₂O₄ lattice based afterglow phosphors, *AIP Conf. Proc.*, 2021, **2352**, 020087.
- 43 R. K. Gartia and M. N. Singh, Deconvolution of thermoluminescence curves and its implications: the case of CaAl₂O₄:Sm³⁺, *Optik*, 2021, **248**, 168048.
- 44 K. S. Chung, J. I. Lee and J. L. Kim, A computer program for the deconvolution of the thermoluminescence glow curves by employing the interactive trap model, *Radiat. Meas.*, 2012, **47**, 766–769.

